



1 **A 2600-yr-long paleoseismic record for the Himalayan Main Frontal Thrust**
2 **(Western Bhutan)**

3

4 Romain Le Roux-Mallouf¹, Matthieu Ferry², Rodolphe Cattin², Jean-François Ritz², Dowchu
5 Drukpa^{2,3}, Phuntsho Pelgay³

6 ¹*Geolithe, Research and Development Department, Rue des Becasses, 38920, Crolles*

7 ²*Géosciences Montpellier, CNRS, UMR5243, Université de Montpellier, Place E. Bataillon,*
8 *34095 Montpellier, France*

9 ³*Seismology and Geophysics Division, Department of Geology and Mines, Post Box 173, 9*
10 *Thimphu, Bhutan*

11



12 **ABSTRACT**

13 In spite of an increasing number of paleoseismic studies carried out over the last decade along
14 the Himalayan arc, the chronology of historical and pre-historical earthquakes is still poorly
15 constrained. In this paper, we present geomorphologic and paleoseismic studies conducted over
16 a large river-cut exposure along the Main Frontal Thrust in southwestern Bhutan. The Piping
17 site reveals a 30-m-high fault-propagation fold deforming late Holocene alluvial deposits.
18 There, we carried out detailed paleoseismic investigations and built a chronological framework
19 on the basis of 22 detrital charcoal samples submitted to radiocarbon dating. Our analysis
20 reveals the occurrence of at least five large and great earthquakes between 485 ± 125 BC and
21 AD 1714 with an average recurrence interval of 550 ± 211 yr. Co-seismic slip values for most
22 events reach at least 13 m and suggest associated magnitudes are in the range of Mw 8.5-9. The
23 cumulative deformation yields an average slip rate of 25.3 ± 4 mm/yr along the Main Frontal
24 Thrust, over the last 2600 yr in agreement with geodetic and geomorphological results obtained
25 nearby.



26 1. INTRODUCTION

27 The Himalayas, accommodating ~50% of the India-Eurasia collision at a shortening rate of ~20
28 mm/yr [e.g. Lavé and Avouac, 2000; Ader et al., 2012; Burgess et al., 2012; Marechal et al.,
29 2016], are a region of sustained seismicity as illustrated recently by the 2015 Mw 7.8 Gorkha
30 earthquake in Nepal [e.g. Avouac et al., 2015; Grandin et al., 2015]. Instrumental and historical
31 records indicate that similar and significantly larger earthquakes have occurred along the
32 Himalayan arc since medieval times [e.g. Rajendran and Rajendran, 2005; Sapkota et al., 2013;
33 Yule et al., 2006; Kumar et al., 2010; Bollinger et al., 2014; Hetenyi et al., 2016]. Records of
34 earlier events are documented as well from man-made and natural paleoseismic exposures (Fig.
35 1a) [e.g. Nakata et al., 1998; Upreti et al., 2000; Lavé et al., 2005; Yule et al., 2006; Kumar et
36 al., 2010; Mugnier et al., 2013; Sapkota et al., 2013; Bollinger et al., 2014; Berthet et al., 2014;
37 Rajendran et al., 2015; Mishra et al., 2016; Le Roux-Mallouf et al., 2016; Wesnousky et al.,
38 2017 ; Wesnousky et al., 2019].

39 A robust estimate of size and recurrence interval needs to extend the time period covered by
40 this catalog of historical events over numerous seismic cycles. With the exception of the study
41 by Bollinger et al. [2014] that yielded five events (and two inferred) from a discontinuous
42 stratigraphic record assembled from four sites, other exposures have only revealed one to two
43 events per site, and a total of a dozen distinct events for the ~2500-km-long Himalayan Arc.
44 Even the Bollinger et al.'s study constitutes a rather short catalog when compared to data
45 available for smaller structures such as the ~1300-km-long San Andreas Fault or the ~1000-
46 km-long Dead Sea Fault or North-Anatolian Fault [e.g. Meghraoui et al., 2012; Rockwell et al.
47 2015]. This issue is mostly due to the accommodation of a high shortening rate along the frontal
48 thrust faults leading to surface ruptures with vertical offsets of up to 10 m [e.g. Kumar et al.,
49 2010; Le Roux-Mallouf et al., 2016] and an average recurrence interval of 500-1000 years [e.g.
50 Bollinger et al., 2014]. Hence, to retrieve long event series, excavations need to reach
51 extraordinarily large dimensions into young unconsolidated deposits, which poses arduous
52 logistics and safety challenges.

53 In this study, in order to investigate large Himalayan earthquake series, we selected a site in
54 southwestern Bhutan where a ~30-m-high natural section is exposed by erosion at the outlet of
55 a trans-Himalayan river called the Wang Chu. After describing the Bhutan Himalaya setting,
56 we present the geomorphological and paleoseismic investigations carried out around and along
57 this exposure. Our results allow us to discuss the timing and the magnitude of five surface-
58 rupturing events that occurred in Bhutan during the last 2600 years.

59



60 2. MORPHOTECTONIC SETTING

61 2.1. Active tectonics in Bhutan

62 From north to south, Bhutan can be divided into four distinct tectonic units (Fig. 1b): the
63 Tethyan Sedimentary Series (TSS), the Higher Himalaya (HH), the lesser Himalaya (LH), and
64 the Siwaliks (Sw). All these units are bounded by major faults including the South Tibetan
65 Detachment (STD), the Main Central Thrust (MCT), the Main Boundary Thrust (MBT), and
66 the Main Frontal Thrust (MFT), which is the most recent expression of the thrust sequence that
67 accommodated the deformation over geological time scales [Gansser, 1964; Le Fort, 1975;
68 McQuarrie et al., 2008; Long et al., 2011a]. At depth, these four major north-dipping thrust
69 faults connect to the Main Himalayan Thrust (MHT), a mid-crustal decollement under which
70 the Indian plate subducts beneath the Himalayas and Tibet. In terms of geometry, several
71 studies suggest a ramp-flat-ramp geometry of the MHT [e.g., Zhao et al., 1993; Nelson et al.,
72 1996; Cattin and Avouac, 2000; Nábelek et al., 2009, Coutand et al., 2014, Le Roux-Mallouf
73 et al., 2015].

74 Present-day deformation is constrained by (1) a far-field convergence of 17 ± 0.5 mm/yr
75 inferred from geodetic measurements along 3 profiles across western, central and eastern
76 Bhutan [Marechal et al., 2016] and (2) a single estimate of Holocene uplift rate of 8.8 ± 2.1
77 mm/yr, from the study of alluvial terraces along the front in central Bhutan [Berthet et al.,
78 2014]. A first paleoseismic study by Le Roux-Mallouf et al. [2016] suggests that south-central
79 Bhutan has been struck by at least two earthquakes during the last millennium, including (1) a
80 Mw 7.5-8.5 earthquake in central Bhutan that produced ~1 m of coseismic uplift in AD 1714
81 [see also Hetényi et al., 2016] and (2) a Mw > 8.5 earthquake that produced ~8 m of coseismic
82 uplift during the medieval times (between AD 1204 and AD 1464). This last event contributes
83 to the debate about the possible deficit of seismic moment along the Himalayan arc [e.g. Bilham
84 et al., 2001; Stevens and Avouac, 2016] and the probability of occurrence of a subduction-type
85 Mw 9 earthquake in this region [Kumar et al., 2010; Mugnier et al., 2013; Srivastava et al.,
86 2013; Stevens and Avouac, 2016, Le Roux-Mallouf et al., 2016, Wesnousky et al., 2017].

87

88 2.2 Geomorphology of the study area

89 The study site, called Piping, is located in the Lhamoizingkha area (SW Bhutan) immediately
90 upstream of the confluence between the Wang Chu and the Ramphu Chu, a 5-km-long tributary
91 that drains a 4.5-km² watershed (Fig. 2a). There, the MFT crosses the Wang Chu (89.759980°E,
92 26.722853°N) and a river-cut exposure reveals geological units and structures (Fig. 2b & 3):



- 93 - *The Lesser Himalayan zone-LH* (Manas Formation, Neoproterozoic-Cambrian) in the
94 north, composed of quartzite, phyllite and dolostone [Long et al., 2011a and references
95 therein] dipping 70-80° to the north;
- 96 - *The Subhimalayan zone-S* (Siwaliks, Miocene-Pliocene), immediately north of the
97 MFT, composed of medium-to-coarse-grained sandstone and pebble-to-cobble-
98 conglomeratic sandstone [Long et al., 2011b et references therein] dipping 50-70° to
99 the north and visible over more than 300 m;
- 100 - *The Alluvial plain*, composed of young unconsolidated sediment.

101 The MFT separates the flat, mostly undeformed, deposits of the Alluvial plain to the south from
102 a well-developed 4-km-long flight of alluvial terraces deposited by the Wang Chu over the
103 Manas and Siwalik formations. These terraces are composed of well-stratified cobbles to
104 boulders (dominant lithology is metamorphic from the Manas Formation) with a sandy matrix.
105 Available outcrops display relatively thin sediment covers (generally less than 6 m) deposited
106 over clear strath surfaces cutting into the Manas and Siwaliks Formations. The lower terraces
107 (T1, T2 and T3) are located directly along the present stream at low relative elevations (~1 m,
108 ~11 m and ~33 m, respectively). T1 and T2 are deposited over the fault trace (Fig. 2a) and
109 display continuous top surfaces suggesting no significant deformation occurred since their
110 deposition. T1 is likely immersed during the monsoon season, as attested by natural and
111 anthropic detritus caught in the low vegetation. Intermediate terraces (T4, T5 and T6) appear
112 as continuous ribbons perched above the present river level at ~43 m, ~80m and ~90 m,
113 respectively. Finally, higher terraces T8 and T9 are strongly dissected and preserved as thick
114 alluvial sequences (e.g. ~18-m-thick for T8) on top of steep buttes forming local heights at
115 ~100 m and ~170 m above the present river level, respectively.

116 East of the study site, a local watershed basin called Ramphu Chu cuts into the Manas and
117 Siwaliks formations and exits the steep piedmont at the location of the MFT where it forms a
118 500-m-wide alluvial fan (Fig. 2a). The upstream section of the fan was deposited against the
119 main MFT tectonic scarp and over the fault trace as visible on field photographs (Fig. 2b and
120 3a) and provides the main stratigraphic section studied here to unravel the recent deformation
121 history along the MFT.

122

123 3. PALEOSEISMIC EXPOSURE

124 An orthorectified photographic mosaic (Fig. 3a) of the site shows the 30-m-high river-cut cliff
125 and displays a 40-m-wide deformation zone that separates the grey Siwaliks (unit S) to the
126 north, topped by the south-dipping U7 terrace (Wang Chu deposits) from an horizontal 18-m-



127 thick sequence of fan deposits (U6 to U0) from the Ramphu Chu. A 50-m-long by 30-m-high
128 section of the natural exposure was cleaned, partly gridded and logged in details (Fig. 3b and
129 following) based on stratigraphy, lithology and grain-size. Overall, 50 samples of organic
130 matter (charcoal and plant debris) were collected, and 22 were selected for radiocarbon age
131 determination (Table 1).

132

133 3.1. Chronostratigraphy

134 The stratigraphy of the northern section of the exposure (Fig. 3) is mostly constituted of
135 massive grey sands with fine beds of white silts, pebbles and cobbles that outline a ~60° dip to
136 the north. This unit crops out along a ~150-m-long section of the river cut and exhibits a
137 thickness of at least 90 m. It is widely observed regionally along the mountain front (Long et
138 al., 2011a) and is attributed to the Siwaliks formation (S). Here, it is overlain with a ~4-m-thick
139 clast-supported stratified cobbles-to-boulders unit (called U7 hereafter). Observed clasts are
140 generally rounded with a significant contribution of metamorphic lithology from the Higher
141 Himalaya formation (Long et al., 2011a). Considering stratigraphy, clasts roundness, distance
142 to the nearest outcrops of said formation (~25 km north of the site) and relationship to the local
143 drainages, we interpret this unit as an alluvial terrace deposit from the trans-Himalayan Wang
144 Chu. Unit U7 is stratigraphically above the Siwaliks (S) and lies over a clear erosion surface
145 (strath) that cuts through the Siwaliks north-dipping stratigraphy. Its top surface is eroded north
146 of grid point (22, 24) and preserved and overlain with a succession of fine-grained units south
147 of it (Fig. 3b); it is hereafter considered to mark the base of the Quaternary stratigraphic record
148 at this site.

149 On top of unit U7, we observed an 18-m-thick succession of deposits comprised of 20-to-40-
150 cm-thick massive bluish-grey silt layers and clast-supported gravel layers with a sandy matrix.
151 Major sediment packages are delimited along continuous near-horizontal (in the undeformed
152 section) limits and named U6 (deepest) to U0 (shallowest). They exhibit abundant detrital
153 charcoal lumps, most of them reaching 1 cm in diameter and displaying freshness, compactness
154 and angularity indicative of *a priori* short transport and storage times. Overall, 50 samples were
155 collected from units U6 to U0, of which 22 were selected and submitted for radiocarbon dating
156 (Table 1). Fine calibration was performed with OxCal 4.2 using a depositional model where
157 samples from the same unit are defined as a phase [*e.g.* Lienkaemper & Bronk Ramsey, 2009]
158 and yielded dates consistent with the observed stratigraphic order.

159 - Unit U6: the lowest unit lies over unit U7 over the northern section of the exposure
160 (north of x=22) where it is ~2 m thick, while its base is presently below the water table in the



161 southern section and could not be logged (Fig. 3). It is comprised of massive fine to very fine
162 silts, blueish grey in color, interbedded with 30-to-40-cm-thick poorly stratified lenses of
163 matrix-supported angular gravels, containing ~50% of fine to coarse sand. The top of U6 is
164 marked by a relatively smooth poorly expressed erosion surface. The age of the unit is
165 constrained by 7 samples with a narrow distribution of radiocarbon ages comprised between
166 2480 ± 30 yr BP and 2625 ± 30 yr BP (Table 1) suggesting a relatively fast deposition process.
167 A single obvious outlier (sample PI-C46 with a radiocarbon age of 37700 ± 800 yr BP) was
168 considered reworked, and therefore discarded from our analysis. Model calibration yields a
169 deposition date of 670 ± 165 BC.

170 - Unit U5: within the southern undeformed section of the exposure section, this unit
171 displays a thickness of ~1.5 m (south of $x=59$ m in Fig. 3b). It exhibits a similar grain-size
172 distribution to that of U6 but with distinct gravel and sand lenses: the bottom section is marked
173 by well-defined fine gravel lenses while the top section is evidenced by a ~1-m-thick coarse
174 sand and gravel lens. The top of unit U5 is defined by a weakly-expressed erosional surface
175 that probably reflects more a short depositional hiatus rather than established rill processes.
176 Unit U5 yielded 6 samples, 4 of which with ages between 2180 ± 30 yr BP and 2285 ± 30 yr
177 BP, again indicative of a relatively fast deposition process. The two remaining samples
178 collected at the base of the unit (PI-C11 and PI-C12) are significantly older than other samples
179 from U5 and even U6 (2905 ± 30 yr BP and 2860 ± 30 yr BP, respectively). We suspect they
180 have been reworked from the lower section of U6 or from an even older unit, and we choose
181 therefore to discard them from our analysis. Model calibration yields a deposition date of 290
182 ± 120 BC.

183 - Unit U4: this unit is 3 to 4 m thick in the southern section of the exposure (south of
184 $x=55$ m in Fig. 3b) and thins out to the north where it forms an onlap against U5 then U6 at
185 $x=38$ m. U4 is almost entirely composed of matrix-supported gravels with a few silt lenses and
186 terminates with a continuous ~15-cm-thick sand layer. This unit did not yield any adequate
187 sample for radiocarbon dating, probably on the account of the higher energy regime at the time
188 of its formation.

189 - Unit U3: this unit displays a very constant thickness of ~1.5 m over the whole exposure
190 (between $x=24$ and $x=98$). It is comprised of massive silts with 20-to-30-cm-thick lenses of
191 coarse sand and fine gravel. U3 yielded 3 samples with radiocarbon ages of 1730 ± 30 yr BP,
192 1960 ± 30 yr BP and 2560 ± 30 yr BP. Since the latter sample is contemporaneous of U6, it is
193 considered reworked and removed from any subsequent analysis. Model calibration yields a
194 deposition date of $AD 240 \pm 100$.



195 - Unit U2: this unit also exhibits a constant thickness of ~1.5 m over the exposure. It is,
196 however, comprised of matrix-supported gravels with a few sand lenses, which suggests a
197 slightly higher energy fluvial regime. It yielded 3 samples with radiocarbon ages 1520 ± 30 yr
198 BP, 1770 ± 30 yr BP and 2405 ± 30 yr BP. Similarly, since the latter is contemporaneous of
199 U6, it is considered reworked and removed from subsequent analysis. Model calibration yields
200 a deposition date of $AD 440 \pm 70$.

201 - Unit U1: this unit is ~3 m thick over the exposure. It displays a stratigraphic content
202 very similar to that of unit U2 and lies over a weak erosional surface forming the top of U2.
203 For logistics and safety reasons, unit U1 could not be sampled for age determination.

204 - Unit U0: this is the ultimate deposit of this section. It displays a variable thickness of
205 ~20 cm to up to 4.5 m with a strongly eroded top surface within the deformed zone, north of
206 $x=52$ m (Fig. 3b). The top of U0 marks the abandonment of the section before it was intensely
207 and almost entirely incised by a local gully ($x=52-70$ m). Although this unit was directly
208 accessed at the location of the uppermost log (box marked “Fig. 8” in Fig. 3), we could not
209 retrieved adequate material for age determination.

210

211 Within this succession, clasts lithology and roundness are constant, thus suggesting a common
212 nearby source for units U6 to U0 distinct from that of U7. Gravels are very angular and made
213 of quartzite and phyllite from the Manas Formation, sands are fine-grained and well classed
214 and silts are massive and blueish gray in color, where not oxidized. Although grain size
215 distribution varies across units from gravel-dominant (with sand lenses) to silt-dominant (with
216 sand and gravel lenses), this does not necessarily reflect significant variations in transport flow
217 velocity [e.g. Miller et al., 2014]. Overall, we interpret units U6 to U0 to derive from the same
218 nearby low-flow-velocity source consistent with the recent alluvial fan mapped at the outlet of
219 the Rampu Chu watershed basin (Fig. 2).

220

221 Two additional units display specific wedge-shaped geometries: W2 between U5 and U4 and
222 W1 deposited against U0 and immediately below the modern soil. Both units exhibit little
223 stratigraphy, intense internal deformation (see details below) and are interpreted as colluvial
224 wedges (more details in the following section). W1 is stratigraphically the youngest unit
225 observed here. Two detrital wood samples (PI-C23 and PI-C24) yield modern ages. Since roots
226 found in the region sometimes resemble tree-trunk bark in terms of size, density and texture,
227 we suspect the ligneous samples PI-C23 and PI-C24 may derive from in-situ roots and may not
228 be representative of W1’s true age. These samples are discarded in our analysis.



229 Additionally, it is quite notable that the undeformed part of the 18-m-thick Ramphu Chu section
230 (south of $x = 54$ in Figure 3b) presents a quasi-continuous (erosion surfaces are poorly
231 expressed and stratigraphic limits are virtually flat) succession of silt, sand and gravel deposits
232 constrained by 15 radiocarbon samples (Table 1). To better assess the timing of deposition for
233 the uppermost units, we assume that deposition was mostly continuous and we build an age-
234 versus-height relationship for all samples retained for our analysis (Figure 4). Our approach
235 yields an average deposition rate of 7.1 ± 0.2 mm/yr between 805 ± 30 BC (U6) and AD 520
236 ± 95 (U2), with potential short-term variability between silt and gravel beds [e.g. Kumar et al.
237 2007]. On that basis, and considering a similar constant sedimentation rate until the final
238 deposition of U0, we may extrapolate the deposition rate and propose a tentative date with large
239 uncertainties (2σ) for the top of U1 at AD 940 ± 200 . Since U0 is strongly eroded, we did not
240 attempt to date its top surface.

241

242 3.2. Exposure description

243 Large-scale deformation across the MFT at the Piping site is illustrated by fault-propagation
244 folding affecting terrace unit U7 shown on Figure 3. U7 crops out ~ 34 m above the present
245 stream (grid point (0, 34) in Fig. 3b), dips increasingly to the south, is sheared by a system of
246 north-dipping thrust fault splays (F2 to F5 in Fig. 3b), dips reverse to the north and disappears
247 underneath a massive 8-to-10-m-thick fault gouge (unit G in Fig. 3b and following). Since U7
248 does not crop out south of the main fault zone, it is necessarily deeper than the present river
249 level (at least below U6) and has hence recorded more than 34 m of uplift since its deposition.
250 Subsequent units U6 to U0 are mostly undeformed from the southernmost tip of the exposure
251 to the center of the studied section (i.e. south of $x = 54$ m in Fig. 3b). There, they exhibit various
252 stages of deformation, from warping with minor faulting (U0 to U3) to folding (U4) and intense
253 faulting with duplexing (U5 and U6), indicating that the older units of the Ramphu Chu fan
254 have cumulated more deformation. Furthermore, fault strand F5 cuts through the whole section
255 and reaches the surface with a near-vertical dip and affects U2 to U0 with an apparent normal
256 geometry. To describe faulting and abutting relationships in detail and identify surface-
257 rupturing events, we focus on two excerpts presented at high resolution in Figures 5 to 8.

258 The lower section documents deformation affecting units U7, U6 and U5 (Fig. 5, 6 and 7).
259 From grid point (28, 2) (Fig. 5b), U7 is overlain with unit (G) composed of massive reddish to
260 brownish clay that contains sheared and fractured clasts from the Siwaliks formation as well as
261 cobbles and boulders from U7. It exhibits intense internal deformation (see close-up in Fig. 7a)
262 typical of a fault gouge. The localized fault contact between G and U7 corresponds to F4 in



263 Fig. 3b and Fig. 5b. To the south, U6 crops out at the base of the exposure and is affected by
264 fault F1, which cuts through U6 and U5, and dies out ~4 m southward within U5 (Fig. 5b). F1
265 accommodates only minor faulting as attested by a relatively small 30-cm offset affecting the
266 base of U5 (Fig. 7b). Secondary normal-geometry splays F6 and F7 branch out from F1 and
267 displace the base of U5 vertically by a total of ~60 cm. F7 tapers out within U5 while F6 cuts
268 it entirely and terminates against the low-dipping fault strand F2 at a right angle. Above F2,
269 U6 displays strongly-deformed near-vertical bedding produced by dragging along F2 (Fig. 6)
270 and forms a fault-propagation fold. Hence, F2 is a duplex fault that accommodates major
271 deformation within the exposure. The uppermost part of unit U6 is affected by similar
272 duplexing deformation along the F3 fault strand, though with a much smaller offset. F2 also
273 affects U5 where duplexing produced a clear scarp overlain with wedge-shaped unit W2. Its
274 stratigraphy is composed of finely-layered silts and gravels similar to U5 but exhibits intense
275 deformation with sheath folds typically associated with slumping along a slope (Fig. 7c), here
276 consistent with the frontal slope of the scarp. We interpret W2 as a scarp-derived colluvial
277 wedge deposited during or shortly after a co-seismic displacement along F2 affecting U5. The
278 top of W2 and U5 are in continuation and overlain by U4, which does not exhibit noticeable
279 deformation at this location and show that F2 was not re-activated after the deposition of U4.
280 The upper section (Fig. 8) documents the northernmost fault strands F4 and F5 as they reach
281 the surface. At the bottom of the trench (Fig. 3b), F4 and F5 originate from the main gouge
282 zone (G) where they dip ~20°N, cut through U7 with a steeper dip of ~50°N and merge together
283 as strand F4/F5, cut through U3 at a near-vertical angle and U2 to U0 with a ~85°S dip. This
284 change of dip angle and direction is expressed within the shallowest units (U3 to U0) by an
285 apparent normal-geometry fault displacement along F4/F5 (see Fig.8b). The detailed log of the
286 upper section shows a ~3-m-wide V-shaped deformation zone bounded by F4/F5 to the north
287 and by a diffuse deformation band affecting U3 to U0 to the south (x = 38-41 m in Figures 3b
288 and 8). In between, units exhibit strong warping and chaotic limits suggesting soft-sediment
289 deformation and collapse against F4/F5. Unit U1 is overlain with U0, which is itself collapsed
290 against F4/F5. The amount of associated vertical displacement is difficult to ascertain, due to
291 the wide collapse zone and the fact that U0 has been eroded north of F4/F5. From the base of
292 the hanging wall section of U1 at grid point (37, 18) to the base of the footwall section of U1
293 at grid point (38.5, 16.5), we estimate a minimum vertical offset of ~1.5 m. Finally, the whole
294 stratigraphic succession is sealed by a ~1.5-m-thick wedge-shaped colluvial unit (W1)
295 deposited over U0 and against what we interpret as F4/F5 free face.
296



297 3.3. Timing of surface ruptures and associated co-seismic displacements

298 In order to identify the various deposition, erosion and deformation events recorded at the
299 Piping site, we propose a schematic sequential retro-deformation combining all observations
300 collected over the exposure (Fig. 9; see Malik et al., 2017, for a similar approach further west).
301 We start from a simplified log (Fig. 9a) and successively retro-deform the whole section to
302 restore the most recent deposits to their original geometry and infer previous events where
303 deformation remains. In parallel, we present OxCal-modeled [Bronk Ramsey, 2009] event
304 dates constrained by 15 radiocarbon samples (see section 3.1) and a chronostratigraphic model
305 following guidelines from Lienkaemper and Bronk Ramsey [2009] (Fig. 10):

306 - Event 1: The most recent deposit observed in the exposure is a ~1.5-m-thick colluvial
307 wedge (W1 in Fig. 8 and 9a) deposited against a free face formed in unit U1 by slip along
308 F4/F5. The diffuse deformation observed within U3, U2 and U1 and the collapse of unit U0
309 within an open fissure are contemporaneous with a first event that occurred after the deposition
310 of U0 (Fig. 8). Radiocarbon-dating of W1 only yielded modern dates (Table 1) -likely due to
311 contamination from actively developing soil- and does not permit to date E1 accurately. From
312 our chronostratigraphic analysis (Fig. 10), E1 occurred after AD 895 and was associated with
313 faulting along faults F4 and F5. Removal of W1 and retro-deformation of units U0 to U3 restore
314 the continuity of the bottom of U0 and leave large-scale folding affecting units U2 and older
315 (given the poor constraint on the size of this first event, which seems a priori small with a
316 minimum displacement of ~1.5 m, we did not represent the stage before event E1).

317 - Event 2: Large-scale folding deforms units U2 to U0 uniformly (Fig. 9a) and indicates
318 a major deformation event affected the stratigraphic section after the deposition of units U2 to
319 U0. Restoring these deposits to their original horizontal geometry (Fig. 9b) in agreement with
320 the southern section of the exposure (Fig. 3b) involves (at least) bringing the highest observable
321 point of unit U1 (erosion surface at grid point (26, 25.5) marked by the northern green star in
322 Fig. 9b) down to the height of U1 top observed in the undeformed section (e.g. grid point (50,
323 14) marked by the southern green star in Fig. 9b). This analysis yields a minimum cumulative
324 (E1+E2) vertical offset of ~11.5 m along the 50-90° north-dipping F4-F5 splay. Considering
325 an average dip of 60° and a co-seismic slip of ~1.5 m for E1, the net co-seismic dip-slip for E2
326 reaches at least 12 m. Furthermore, our chronostratigraphic model (Fig. 10) yields the same
327 time window for the occurrence of E2 as for E1, i.e. after AD 895. Removing the now
328 undeformed units U2 to U0 reveals that significant folding and faulting remain for units U3
329 and older (Fig. 9c).



330 - Event 3: By applying the same approach to units U4 and U3 and considering that the
331 uppermost point of the top of unit U3 has been eroded away, we estimate the height difference
332 between grid point (26, 25.5) and the height of the top of U3 in the undeformed section, to be
333 9.5 m (blue stars in Fig. 9c). This yields a minimum cumulative vertical offset along F3, F4
334 and F5 of ~16 m for E3+E2+E1, hence ~4.5 m of vertical offset for E3 alone. Since slip
335 propagated primarily along F3 with an average dip of ~20°, we estimate the co-seismic dip-
336 slip for E3 along F4 at ~13.2 m. U3 is the youngest affected unit, while U2 is the oldest
337 unaffected unit, which indicates E3 occurred between the deposition of U3 and U2. Our
338 radiocarbon chronology (Fig. 10) yields a date of occurrence at AD 300 ± 70. Retro-
339 deformation along F3, then removal of undeformed units U4 and U3 suggests residual
340 deformation affects units U5 and older (Fig. 9d).

341 - Event 4: At this stage (Fig. 9e), units U5 and U6 form a ~2-m-high scarp on the ground
342 surface rapidly covered by scarp-derived colluvium W2 at the toe of the scarp. In Figures 3 and
343 5, the U5 package located underneath F2 between $x=33.5$ m and $x=38$ m only exhibits the
344 lower part of U5 (units U5b and U5c) while the duplexed part above F2 only exhibits the upper
345 section of U5 (U5a). Hence, restoring U5 involves removing W2 then retro-sliding the
346 duplexed part of U5 along F2 to bring grid point (51.5, 5) back to its minimal original position
347 at grid point (39.5, 4) with a dip-slip offset of ~13.5 m along F2. In parallel, minor
348 displacements along F1 (~30 cm reverse faulting, see Fig. 7b), F6 (~25 cm normal faulting)
349 and F7 (~35 cm normal faulting) accommodate the anticlockwise rotation of a ~10 m long
350 block of U5 and U6 underneath F2, likely associated with pure shear deformation under the
351 weight of the propagating fold (see Fig. 5b). This event is predated by the deposition of U5 and
352 postdated by the deposition of U4, hence bracketed at 100 ± 160 BC (Fig. 10). This brings U5
353 to its original undeformed geometry forming a near horizontal unit deposited against a pre-
354 existing scarp formed in U6, as attested by the onlap termination visible at grid point (38, 13)
355 in Figure 3a.

356 - Event 5: This event is documented by the remaining scarp affecting U6 once previous
357 events are retro-deformed and U5 is removed (Fig. 9g). Although the height of this scarp is
358 poorly constrained, the retro-deformation analysis suggests it is at least 2 m high and was
359 produced by slip along a shallow-dipping rupture (~10°N), similar to F2 and F3 as observed at
360 the base of the exposure (below $z=1$ m). Hence, we propose that the amount of slip involved
361 during E5 is similar to what is inferred for E4. Furthermore, since the event took place between
362 the deposition of units U6 and U5, it may be dated back to 485 ± 125 BC (Fig. 10).

363



364 A striking feature of surface deformation visible in the Piping exposure is the gradual change
365 in fault dip over time. While all fault strands converge and dip 35-40°N below grid point (30,
366 2) they diverge from ~10°N to ~50°N (locally 90°) as they propagate to the south (Fig. 3 and
367 Fig. 9), presenting a geometry similar to tri-shear folding [Allmendinger, 1998]. In detail, the
368 oldest event (E5) occurred while the top of unit U6 constituted the ground surface (i.e. the event
369 horizon) and is expressed along a shallow 10° north-dipping duplex rupture. The situation is
370 similar for E4. After deposition of units U4 and U3 adding 2.5-3 m of sediments on top of the
371 E5 rupture, the following event (E3) emerges higher in the stratigraphic section along F3 with
372 a steeper dip of 25-30°. A consequent deposition episode adds at least 8.5 m of sediments (units
373 U2, U1 and U0) over these ruptures. The most recent event(s) (E2 and E1) exhibit a much
374 steeper rupture (along strands F4 and F5) with a dip reaching ~50° within unit U7 (coarse-
375 grained terrace deposits) and 90° as it emerges to the present-day surface through unit U0 (fine-
376 grained fan deposits).

377 It is a common observation both in the field and in analog experiments that ruptures along
378 thrust faults tend to flatten as they reach the surface under the influence of decreasing lithostatic
379 pressure [e.g. Philip and Meghraoui, 1983; Lee et al., 2001]. We propose that the change in
380 deformation style from nearly horizontal (E5 and E4) to steep (E2) then vertical (E1) displayed
381 in the Piping trench reflects increasing vertical load onto the foot of the tectonic scarp
382 associated with the progressive buildup of the Rampu Chu fan against it.

383

384

385 **4. SUMMARY OF RECURRENCE TIMES, MAGNITUDES AND SLIP RATE**

386 Paleoseismic investigations conducted along the MFT at the confluence between the Wang
387 Chu and the Ramphu Chu in Western Bhutan show an important cumulative deformation zone
388 including a rich chronology of deposition phases and deformation events for the last ~2600
389 years.

390 The most recent event (E1) is consistent in terms of amount of co-seismic slip and
391 chronology with the most recent event identified by Berthet et al. [2014] and Le Roux-Mallouf
392 et al. [2016] in the Sarpang area (~50 km to the east, see Fig. 11) and interpreted as the AD
393 1714 earthquake (previously described as the AD 1713 earthquake by Ambraseys and Jackson,
394 2003). By combining historical and paleoseismic constraints, Hétényi et al. [2016] propose that
395 this earthquake reached Mw 7.5-8.5 with a modeled rupture centered on Bhutan and largely
396 encompassing the Piping site. We therefore propose that E1 corresponds to the AD 1714
397 earthquake. Similarly, our event E2 is consistent with an event observed at the Sarpang site as



398 well dated AD 1344 ± 130 (Fig. 11) and tentatively associated with a medieval earthquake that
399 may have ruptured a large section of the MFT (see Le Roux-Mallouf et al., 2016 and references
400 therein). Hence, we propose that our event E2 corresponds to that second event. Events E3, E4,
401 and E5 occurred at AD 300 ± 70 , 100 ± 160 BC, and 485 ± 125 BC, respectively.

402 Hence, according to our retro-deformation analysis and chronostratigraphic model, our results
403 allow constraining the occurrence of five surface-rupturing events between 485 ± 125 BC and
404 AD 1714 with an average recurrence interval of 550 ± 211 yr. When only considering events
405 with the largest documented co-seismic slip values (E2 to E5) that are the most likely to be
406 preserved and observed in exposures, the average recurrence interval reaches 610 ± 238 yr.
407 Ours results are comparable to the lower values obtained for the late Holocene by Bollinger et
408 al. [2014] in eastern Nepal (610 to 1220 yr, depending on hypotheses). Furthermore, the
409 relatively small co-seismic slip value determined for E1 (and assigned to the AD 1714
410 earthquake) suggests smaller though destructive events may occur on occasion as was the case
411 for the 2015 Gorkha earthquake in Central Nepal [e.g. Grandin et al., 2015] although there was
412 no surface rupture associated with it.

413 The retro-deformation analysis also allows estimating associated dip-slip co-seismic
414 displacements with values ranging from ~ 1.5 m for E1 to more than 13 m for E2, E3, E4 and
415 probably E5, a value typical of the largest events documented along the Himalayas in Nepal,
416 Sikkim, Bhutan and Assam and consistent with extreme magnitudes on the order of M_w 9 (Le
417 Roux-Mallouf et al., 2016 and references therein). Considering the largest events, this
418 represents ~ 40.2 m of slip (E2+E3+E4) accrued over 1629 ± 255 yr (between E5 and E2) at a
419 rate of 25.3 ± 4 mm/yr. Although the duration of our dataset may be too limited to represent
420 the long term behavior of the MFT, this slip rate is consistent with those derived from 8-kyr-
421 old uplifted terraces in Sarpang (Fig. 11) [Berthet et al., [2014] and from far-field GPS
422 shortening rate measurements [Marechal et al., 2016]. Together, these results suggest that the
423 Himalayan convergence is mainly seismically accommodated along the MFT in western
424 Bhutan as well.

425
426

427 5. CONCLUSION

428 We presented here the longest continuous record of paleo-earthquakes along the Himalayan
429 arc from the detailed study of an 18-m-thick deformed sedimentary sequence dated from 15
430 radiocarbon samples. Well-expressed deformation and a detailed retro-deformation analysis
431 reveal the occurrence of five surface-rupturing earthquakes along the MFT in southwestern



432 Bhutan during the past ~2600 years. The two most recent events can be related to the AD 1714
433 earthquake [Hétényi et al., 2016] and a medieval event (AD 1344 ± 130) already described in
434 south central Bhutan [Le Roux-Mallouf et al., 2016]. More strikingly, events E3, E4 and E5
435 are documented here for the first time and constitute some of the oldest paleoearthquakes
436 characterized in the Central Himalayas (Fig. 11). Together, these events give an average
437 earthquake recurrence interval of 550 ± 211 yr (or 610 ± 238 yr for the largest) for the Main
438 Frontal Thrust in Bhutan.

439 The slip rate of 25.3 ± 4 mm/yr obtained from cumulative slip is consistent with both Holocene
440 rates obtained from uplifted terraces [Berthet et al., 2014] and high interseismic coupling level
441 inferred from geodetic measurements [Marechal et al., 2016], which suggests that the
442 Himalayan convergence in western Bhutan is mainly seismically accommodated along the
443 MFT. Moreover, this result suggests that –at least locally- the slip budget does not display
444 significant deficit over the time period of this study [Stevens and Avouac, 2016]. Finally,
445 estimated co-seismic displacements between ~1.5 m and at least 13 m indicate the occurrence
446 of large (between Mw ~7.5 and Mw ~8.5) and great earthquakes (MW > 8.5) at a single site.
447 This complexity should be taken into account in probabilistic seismic hazard calculations.

448

449 **Author contribution**

450 RLM, MF, JFR and PP conducted field work. RLM and MF prepared the manuscript with
451 contributions from all co-authors.

452

453 **Competing interests**

454 The authors declare that they have no conflict of interest.

455

456 **ACKNOWLEDGMENTS**

457 This project is funded by the French Agence Nationale de la Recherche (ANR-13-BS06-0006-
458 01) and CNES (Pleiades satellite images and field support). We would like to thank all people
459 helping in the field and particularly our driver Phajo Kinley from the Department of Geology
460 and Mines. We also thank S. Dominguez (Géosciences Montpellier) for fruitful discussions.
461 Correspondence and requests for materials should be addressed to
462 romain.lerouxmallouf@geolithe.com

463



464 **REFERENCES**

- 465 Ader, T., et al. (2012), Convergence rate across the Nepal Himalaya and interseismic coupling
466 on the Main Himalayan Thrust: Implications for seismic hazard, *J. Geophys. Res.*, 117,
467 B04403. doi:10.1029/2011JB009071.
- 468 Allmendinger, R.W. 1998. Inverse and forward numerical modeling of trishear fault-
469 propagation folds. *Tectonics*, 17, 640-656. doi: 10.1029/98tc01907.
- 470 Ambraseys, N., and D. Jackson (2003), A note on early earthquakes in northern India and
471 southern Tibet, *Curr. Sci.*, 84, 570–582.
- 472 Avouac, J.-P., L. Meng, S. Wei, T. Wang, and J.-P. Ampuero (2015), Lower edge of locked
473 Main Himalayan Thrust unzipped by the 2015 Gorkha earthquake. *Nature Geoscience*, 8(9),
474 708–711, doi:10.1038/ngeo2518.
- 475 Berthet, T., J.F. Ritz, M. Ferry, P. Pelgay, R. Cattin, D. Drukpa, R. Braucher, and G. Hetényi
476 (2014), Active tectonics of the eastern Himalaya: New constraints from the first tectonic
477 geomorphology study in southern Bhutan, *Geology*, 42(5), 427-430, doi:10.1130/G35162.1.
- 478 Bilham, R., Gaur, V. K., & Molnar, P. (2001). Himalayan seismic hazard. *Science*, 293(5534),
479 1442-1444.
- 480 Bollinger, L., S. N. Sapkota, P. Tapponnier, Y. Klinger, M. Rizza, J. Van der Woerd, D. R.
481 Tiwari, R. Pandey, A. Bitri, and S. Bes de Berc (2014), Estimating the return times of great
482 Himalayan earthquakes in eastern Nepal: Evidence from the Patu and Bardibas strands of
483 the Main Frontal Thrust, *J. Geophys. Res. Solid Earth*, 119(9), 7123–7163,
484 doi:10.1002/2014JB010970.
- 485 Burgess, W. P., Yin, A., Dubey, C. S., Shen, Z. K., & Kelty, T. K. (2012). Holocene shortening
486 across the Main Frontal Thrust zone in the eastern Himalaya. *Earth and Planetary Science*
487 *Letters*, 357, 152-167.
- 488 Bronk Ramsey, C. (2009). Bayesian analysis of radiocarbon dates. *Radiocarbon*, 51(1), 337-
489 360.
- 490 Cattin, R., & Avouac, J. P. (2000). Modeling mountain building and the seismic cycle in the
491 Himalaya of Nepal. *Journal of Geophysical Research: Solid Earth*, 105(B6), 13389-13407.
- 492 Coutand, I., D. M. Whipp Jr., D. Grujic, M., Bernet, M. G. Fellin, B. Bookhagen, K. R., Landry,
493 S. K. Ghalley, and C. Duncan (2014), Geometry and kinematics of the Main Himalayan
494 Thrust and Neogene crustal exhumation in the Bhutanese Himalaya derived from inversion
495 of multithermochronologic data, *J. Geophys. Res. Solid Earth*, 119, 1446–1481,
496 doi:10.1002/2013JB010891.
- 497 Gansser, A., 1964. *Geology of the Himalayas*, Wiley Interscience.



- 498 Grandin, R., M. Vallée, C. Satriano, R. Lacassin, Y. Klinger, M. Simoes, and L. Bollinger
499 (2015), Rupture process of the Mw = 7.9 2015 Gorkha earthquake (Nepal): Insights into
500 Himalayan megathrust segmentation, *Geophys. Res. Lett.*, 42(20), 8373–8382,
501 doi:10.1002/2015GL066044.
- 502 Grujic, D., C. J. Warren, and J. L. Wooden (2011), Rapid synconvergent exhumation of
503 Miocene-aged lower orogenic crust in the eastern Himalaya, 346–366, doi:10.1130/L154.1.
- 504 Hetényi, G., Roux-Mallouf, L., Berthet, T., Cattin, R., Cauzzi, C., Phuntsho, K., & Grolimund,
505 R. (2016). Joint approach combining damage and paleoseismology observations constrains
506 the 1714 AD Bhutan earthquake at magnitude 8 ± 0.5 . *Geophysical Research Letters*, 43(20).
- 507 Kumar, R., Suresh, N., Sangode, S. J., & Kumaravel, V. (2007). Evolution of the Quaternary
508 alluvial fan system in the Himalayan foreland basin: Implications for tectonic and climatic
509 decoupling. *Quaternary International*, 159(1), 6–20.
- 510 Kumar, S., Wesnousky, S. G., Jayangondaperumal, R., Nakata, T., Kumahara, Y., & Singh, V.,
511 (2010). Paleoseismological evidence of surface faulting along the northeastern Himalayan
512 front, India: Timing, size, and spatial extent of great earthquakes, *J. Geophys. Res. Solid*
513 *Earth*, 115(B12), 1–20, doi:10.1029/2009JB006789.
- 514 Lavé, J., & Avouac, J. P. (2000). Active folding of fluvial terraces across the Siwaliks Hills,
515 Himalayas of central Nepal. *Journal of Geophysical Research: Solid Earth*, 105(B3), 5735–
516 5770.
- 517 Lavé, J., Yule, D., Sapkota, S., Basant, K., Madden, C., Attal, M., & Pandey, R., (2005).
518 Evidence for a great medieval earthquake (~1100 AD) in the central Himalayas, Nepal.
519 *Science*, 307(5713), 1302–1305, doi:10.1126/science.1104804.
- 520 Le Fort, P., (1975), Himalaya: the collided range. Present knowledge of the continental arc,
521 *Am. J. Sci.*, 275, 1–44.
- 522 Le Roux-Mallouf, R., V. Godard, R. Cattin, M. Ferry, J. Gyeltshen, J.-F. Ritz, D. Drupka, V.
523 Guillou, M. Arnold, G. Aumaître, D. L. Bourlès, and K. Keddadouche (2015), Evidence for
524 a wide and gently dipping Main Himalayan Thrust in western Bhutan. *Geophys. Res. Lett.*,
525 42, 3257–3265. doi:10.1002/2015GL063767.
- 526 Le Roux-Mallouf, R., Ferry, M., Ritz, J. F., Berthet, T., Cattin, R., & Drukpa, D. (2016). First
527 paleoseismic evidence for great surface-rupturing earthquakes in the Bhutan Himalayas.
528 *Journal of Geophysical Research: Solid Earth*, 121(10), 7271–7283.
- 529 Lee, J.-C., Chen, Y.-G., Sieh, K., Mueller, K., Chen, W.-S., Chu, H.-T., Chan, Y.-C., Rubin,
530 C., Yeats, R. (2001). A Vertical Exposure of the 1999 Surface Rupture of the Chelungpu



- 531 Fault at Wufeng, Western Taiwan: Structural and Paleoseismic Implications for an Active
532 Thrust Fault. *Bull. Seism. Soc. Am.*, 91, 914-929, doi: 10.1785/0120000742.
- 533 Lienkaemper, J. J., & Bronk Ramsey, C. (2009). OxCal: Versatile Tool for Developing
534 Paleoearthquake Chronologies - A Primer. *Seismological Research Letters*, 80(3), 431-434,
535 doi:10.1785/gssrl.80.3.431.
- 536 Long, S., McQuarrie, N., Tobgay, T., Grujic, D. and Hollister, L. (2011a) Geologic Map of
537 Bhutan, *Journal of Maps*, 7(1), 184-192, doi: 10.4113/jom.2011.1159.
- 538 Long, S., McQuarrie, N., Tobgay, T., Rose, C., Gehrels, G., & Grujic, D. (2011b).
539 Tectonostratigraphy of the Lesser Himalaya of Bhutan: Implications for the along-strike
540 stratigraphic continuity of the northern Indian margin. *Geological Society of America*
541 *Bulletin*, 123(7-8), 1406-1426.
- 542 Malik, J.N., Naik, S.P., Sahoo, S., Okumura, K., Mohanty, A. (2017). Paleoseismic evidence
543 of the CE 1505 (?) and CE 1803 earthquakes from the foothill zone of the Kumaon Himalaya
544 along the Himalayan Frontal Thrust (HFT), India. *Tectonophysics*, 714-715, 133-145.
545 doi:10.1016/j.tecto.2016.07.026
- 546 Marechal, A., Mazzotti, S., Cattin, R., Cazes, G., Vernant, P., Drukpa, D., ... & Pelgay, P.
547 (2016). Evidence of interseismic coupling variations along the Bhutan Himalayan arc from
548 new GPS data. *Geophysical Research Letters*.
- 549 McQuarrie, N., Robinson, D., Long, S., Tobgay, T., Grujic, D., Gehrels, G., Ducea, M., (2008),
550 Preliminary stratigraphic and structural architecture of Bhutan: Implications for the along
551 strike architecture of the Himalayan system: *Earth and Planetary Science Letters*, 272(1),
552 105-117, doi: 10.1016/j.epsl.2008.04.030.
- 553 Meghraoui, M., Aksoy, M. E., Akyüz, H. S., Ferry, M., Dikbaş, A., & Altunel, E. (2012).
554 Paleoseismology of the North Anatolian fault at Güzelköy (Ganos segment, Turkey): Size
555 and recurrence time of earthquake ruptures west of the Sea of Marmara. *Geochemistry,*
556 *Geophysics, Geosystems*, 13(4).
- 557 Miller, K.L., Reitz, M.D. & Jerolmack, D.J. (2014). Generalized sorting profile of alluvial fans.
558 *Geophysical Research Letters*, 41, 7191-7199. doi: 10.1002/2014gl060991.
- 559 Mishra, R. L., Singh, I., Pandey, A., Rao, P. S., Sahoo, H. K., & Jayangondaperumal, R. (2016).
560 Paleoseismic evidence of a giant medieval earthquake in the eastern Himalaya. *Geophysical*
561 *Research Letters*, 43(11), 5707-5715.
- 562 Mugnier, J.-L., Gajurel, A., Huyghe, P., Jayangandaperumal, R., Jouanne, F., Upreti, B.,
563 (2013), Structural interpretation of the great earthquakes of the last millennium in the central
564 Himalaya, *Earth Science Reviews*, 127, 30-47, doi: 10.1016/j.earscirev.2013.09.003.



- 565 Nakata, T., Kumura, K., & Rockwell, T. (1998). First successful paleoseismic trench study on
566 active faults in the Himalaya. *Eos Trans. AGU*, 79, 45.
- 567 Nelson, K. D., Zhao, W., Brown, L. D., & Kuo, J. (1996). Partially molten middle crust beneath
568 southern Tibet: synthesis of project INDEPTH results. *Science*, 274(5293), 1684.
- 569 Philip H., and Meghraoui, M. (1983). Structural analysis and interpretation of the surface
570 deformations of the El Asnam Earthquake of October 10, 1980. *Tectonics*, 2, 17-49. doi:
571 10.1029/TC002i001p00017.
- 572 Rajendran, C. P., and K. Rajendran (2005), The status of central seismic gap: a perspective
573 based on the spatial and temporal aspects of the large Himalayan earthquakes,
574 *Tectonophysics*, 395(1), 19–39, doi:10.1016/j.tecto.2004.09.009.
- 575 Rajendran, C. P., B. John, and K. Rajendran (2015), Medieval pulse of great earthquakes in the
576 central Himalaya: Viewing past activities on the frontal thrust, *J. Geophys. Res. Solid Earth*,
577 120(3), 1623–1641 doi:10.1002/2014JB011015.
- 578 Rockwell, T. K., Dawson, T. E., Ben-Horin, J. Y., & Seitz, G. (2015). A 21-event, 4,000-year
579 history of surface ruptures in the Anza seismic gap, San Jacinto Fault, and implications for
580 long-term earthquake production on a major plate boundary fault. *Pure and Applied*
581 *Geophysics*, 172(5), 1143-1165.
- 582 Sapkota, S. N., Bollinger, L., Klinger, Y., Tapponnier, P., Gaudemer, Y., & Tiwari, D., (2013).
583 Primary surface ruptures of the great Himalayan earthquakes in 1934 and 1255. *Nature*
584 *Geoscience*, 6(2), 71-76, doi:10.1038/ngeo1669.
- 585 Srivastava, H. N., B. K. Bansal, and Mithila Verma (2013), Largest earthquake in Himalaya:
586 An appraisal, *Journal of the Geological Society of India*, 82.1, 15-22.
- 587 Stevens, V. L., and J.-P. Avouac (2016), Millenary Mw > 9.0 earthquakes required by geodetic
588 strain in the Himalaya, *Geophys. Res. Lett.*, 43, 1118 – 1123, doi:10.1002/2015GL067336.
- 589 Upreti, B. N., Nakata, T., Kumahara, Y., Yagi, H., Okumura, K., Rockwell, T. K., Viridi, N.S.,
590 & Maemoku, H. (2000). The latest active faulting in southeast Nepal. *Active Fault Research*
591 *for the New Millennium*, 533-536.
- 592 Yule, D., J. Lave, S. N. Sapkota, D. Tiwari, B. Kafle, M. R. Pandey, S. Dawson, C. Madden,
593 and M. Attal (2006), Large surface rupture of the Main Frontal Thrust in east-central and
594 western Nepal-Evidence for an unprecedented type of Himalayan earthquake, *Proceedings*
595 *on the International Workshop on Seismology, seismotectonics and seismic hazard in the*
596 *Himalayan region, Kathmandu, 28–29 November, 2006, 13–14.534.*



597 Wesnousky, S. G., Kumahara, Y., Chamlagain, D., Pierce, I. K., Karki, A., & Gautam, D.
598 (2017). Geological observations on large earthquakes along the Himalayan frontal fault near
599 Kathmandu, Nepal. *Earth and Planetary Science Letters*, 457, 366-375.
600 Wesnousky, S. G., Kumahara, Y., Chamlagain, D., & Neupane, P. C. (2019). Large Himalayan
601 Frontal Thrust paleoearthquake at Khayarmara in Eastern Nepal. *Journal of Asian Earth*
602 *Sciences*, 174, 346-351.
603
604
605



606

607 **TABLE**

608

609 **Table 1.** AMS Radiocarbon (^{14}C) dates from detrital charcoals collected from the Piping
610 exposure. Samples in italics were discarded from our analysis (see main text for details).

611 ^aSee trench log for stratigraphic unit designations.

612 ^bRadiocarbon years B.P. relative to 1950 AD (with 1σ counting error). All samples have been dated by the
613 Poznan Radiocarbon Laboratory.

614 ^cCalendric dates were calibrated using OxCal and the atmospheric calibration curve IntCal13. Calendric ages
615 have been rounded to the nearest $\frac{1}{2}$ decade assuming the 5 years accuracy of the IntCal13 curve. D Calendric
616 dates were calibrated using the atmospheric calibration curve IntCal09 for the Northern Hemisphere

617

618 **FIGURE CAPTIONS**

619 **Figure 1**

620 Location of the study area and its regional context. Inset shows the location of Bhutan along
621 the Himalayan arc. (A) Himalayan arc. Red stars are epicenters of great and large earthquakes
622 from instrumental, historical and paleoseismic studies. Orange rectangles are previous
623 paleoseismic studies (a) Mohana Khola [Yule et al., 2006]; (b) Koilabas Khola [Mugnier et al.,
624 2011]; (c & d) Tribeni and Bagmati [Wesnousky et al., 2017]; (e) Sir Bardibas [Sapkota et al.,
625 2013; Bollinger et al., 2014]; (f) Khayarmara [Wesnousky et al., 2019]; (g) Marha Khola [Lavé
626 et al., 2005]; (h) Hokse [Nakata et al., 1998, Upreti et al., 2000]; (i) Panijhora [Mishra et al.,
627 2016] (j) Chalsa [Kumar et al., 2010]; (k) Sarpang [Le Roux-Mallouf et al., 2016]; (l) Nameri
628 [Kumar et al., 2010]; (m) Harmutty [Kumar et al., 2010]. The blue rectangle is the location of
629 the paleoseismic study presented in this paper. (B) North-south simplified geological cross
630 section across western Bhutan (modified after Grujic et al., [2011]). See Figure 1A for location,
631 dashed line labeled “b”. Abbreviations are as follows: TSS, Tethyan Sedimentary Sequence;
632 HH, Higher Himalayan; LH, Lesser Himalayan; Sw, Siwaliks sediments; GP, Ganga Plain;
633 STD, Inner South Tibetan Detachment; KT, Kakhtang Thrust; MCT, Main Central Thrust;
634 MBT, Main Boundary Thrust; MFT, Main Frontal Thrust.

635

636 **Figure 2**

637 Geomorphological map of the study area. (A) Geomorphological map of the Main Frontal
638 Thrust, in the Piping area, superimposed on 2-m-resolution Pleiades-derived Digital Elevation



639 Model. Alluvial terraces are labeled from T0 (active channel) to T8 (oldest). Camera pictogram
640 indicates the location of the panorama in B. White star indicates the location of the Piping
641 exposure. Spacing of elevation contours is 20 m. Black dots indicate spot elevations extracted
642 from an in-house Pleiades DEM. (B) Panorama photography (eastward view) of the large scale
643 Piping site including the southern Piping exposure.

644

645 **Figure 3**

646 Piping paleoseismic exposure. (A) Orthorectified photomosaic of the left-bank of the Wang
647 Chu (southernmost section of Fig. 2b) showing the contact between the Siwalik units (light
648 grey) and Rampu Chu fan deposits (well-stratified beige to grey units). White rectangles
649 indicate the locations of Fig. 5, 7 and 8. (B) Detailed log over a 2-m grid. Solid and dashed red
650 lines are main faults (certain and suspected, respectively). Blue squares indicate the locations
651 and 2σ -calibrated calendar ages of 22 detrital charcoal samples. Samples in italics were
652 discarded from our analysis (see main text for details). The lower 1.5 m of the exposure is here
653 hidden by the access path built by the backhoe.

654

655 **Figure 4**

656 Evolution of age versus height for the Ramphu Chu sedimentary sequence. Data (black outline
657 diamonds) describes a satisfactory linear regression ($R^2 = 0.95$) and allows interpolating
658 towards present. Modelled points (red outline diamonds) and 2σ variance determined from the
659 height of sedimentary limits suggest the top of U1 was deposited at $AD\ 940 \pm 200$. Associated
660 uncertainties are deduced from the 2σ curves.

661

662 **Figure 5**

663 Lower part of Piping paleoseismic exposure. (A) Orthorectified photomosaic of the left-bank
664 of the Wang Chu. White rectangles indicate the location of figures 6 and 7 (a, b and c). (B)
665 Detailed log over a 1-m grid. Solid and dashed red lines are main faults (certain and suspected,
666 respectively). Blue squares indicate the locations and 2σ -calibrated calendar ages of 22 detrital
667 charcoal samples. Samples in italics were discarded from our analysis (see main text for
668 details).

669



670 **Figure 6**

671 Enlarged photograph of the lower part of the exposure (see Fig. 5a for location) showing (1)
672 sub-horizontal deposits of U5 and U6 below the thrust fault F2 and (2) the overturned limb of
673 U6 and U7 characterized by tilted gravel and silty layers and pebbles, respectively.

674

675 **Figure 7**

676 Enlarged ortho-photographies showing (A) the northward-dipping-contact between the gouge
677 fault G and the overturned alluvial terrace U7 at the bottom of the exposure, (B) the 50-cm-
678 offset and the shear texture induced by the fold termination of the F1 thrust fault at the southern
679 end of the deformation zone and (C) a slump figure within the colluvial wedge W2 associated
680 with event E4 along fault splays F1 and F2.

681

682 **Figure 8**

683 Upper part of the Piping paleoseismic exposure. (A) Orthorectified photomosaic of the left-
684 bank of the Wang Chu showing fault F4/F5 (B) Detailed log over a 1-m grid. Solid and dashed
685 red lines are main faults (certain and suspected, respectively). F4/F5 is associated with a
686 vertical fabric, affects all alluvial units and is capped by colluvial wedge W1. Blue squares
687 indicate the locations and calendar ages of 2 detrital charcoal samples.

688

689 **Figure 9**

690 Sequentially restored cross section illustrating the chronology of the successive deposition and
691 deformation episodes at the Piping site. All ages are derived from an OxCal chronostratigraphic
692 model.

693

694 **Figure 10**

695 Chrono-stratigraphic model for deposition episodes (alluvial units U0 to U6 and colluvial
696 wedge W1) and surface-rupturing events (E5 to E1) at the Piping exposure. The model is built
697 from abutting relationships between stratigraphy and faulting and is constrained by 18 detrital
698 charcoal samples and one inferred age corresponding to the top of unit U1. All resulting
699 calendar dates are rounded to the nearest multiple of 5.

700

701 **Figure 11**

702 (A) Synthesis of available paleoseismic records along the Himalayan Arc. (B) Synoptic
703 calendar and positions of great/large earthquakes along the Himalayan front (including



704 instrumental, historical and paleoseismic events). Orange horizontal bars approximate
705 minimum source lengths with or without observed surface rupture. Vertical blue bars
706 correspond to the radiocarbon-model constraints on the timing of the different events. Vertical
707 brown bars correspond to ~2600-yr-long record deduced from the present study.



Unit	Sample name	Nature	Measured radiocarbon age (years B.P.)	Calibrated ages (Calendric, 2σ)	C [mg]	δ ¹³ C value
W1	PI-C24	bark	140.6 ± 0.44 pMC	modern	1.20	-28.8
W1	PI-C23	bark	118.29 ± 0.31 pMC	modern	3.60	-25.9
U2	PI-C43	charcoal	1520 ± 30	AD 520 ± 95	1.08	-24.7
U2	PI-C35	charcoal	1770 ± 30	AD 330 ± 60	0.39	-33.1
U2	<i>PI-C33</i>	<i>charcoal</i>	<i>2405 ± 30</i>	<i>BC 565 ± 160</i>	<i>1.00</i>	<i>-29.1</i>
U3	PI-C37	charcoal	1730 ± 30	AD 240 ± 100	1.77	-30.3
U3	PI-C40	charcoal	1960 ± 30	AD 45 ± 85	0.87	-27.9
U3	<i>PI-C38</i>	<i>charcoal</i>	<i>2560 ± 30</i>	<i>BC 680 ± 125</i>	<i>0.77</i>	<i>-26.1</i>
U5	PI-C09	charcoal	2180 ± 30	BC 270 ± 100	1.26	-27.6
U5	PI-C19	charcoal	2240 ± 30	BC 300 ± 95	2.62	-31.3
U5	PI-C28	charcoal	2285 ± 30	BC 310 ± 100	2.01	-31.8
U5	PI-C16	charcoal	2280 ± 30	BC 310 ± 100	1.91	-30.6
U5	<i>PI-C11</i>	<i>charcoal</i>	<i>2905 ± 30</i>	<i>BC 1110 ± 100</i>	<i>0.89</i>	<i>-28.8</i>
U5	<i>PI-C12</i>	<i>charcoal</i>	<i>2860 ± 30</i>	<i>BC 1025 ± 95</i>	<i>0.86</i>	<i>-28.1</i>
U6	PI-C06	charcoal	2495 ± 30	BC 660 ± 125	1.87	-26.3
U6	PI-C05	charcoal	2485 ± 35	BC 645 ± 140	1.90	-29.6
U6	PI-C36	charcoal	2510 ± 30	BC 665 ± 125	2.55	-22.7
U6	PI-C42	charcoal	2480 ± 30	BC 645 ± 135	1.67	-20.8
U6	PI-C44	charcoal	2590 ± 30	BC 710 ± 115	1.04	-32.1
U6	PI-C48	charcoal	2545 ± 30	BC 675 ± 130	1.17	-27.5
U6	PI-C29	charcoal	2625 ± 30	BC 805 ± 30	1.26	-26.8
U6	<i>PI-C46</i>	<i>charcoal</i>	<i>37700 ± 800</i>	<i>BC 40080 ± 1280</i>	<i>0.59</i>	<i>-28.4</i>

^aSee trench log for stratigraphic unit designations.

^bRadiocarbon years B.P. relative to 1950 A.D. (with 1 σ counting error). All samples have been dated by the Poznan Radiocarbon Laboratory.

^cCalendric dates were calibrated using OxCal and the atmospheric calibration curve IntCal13. Calendric ages have been rounded to the nearest ½ decade assuming the 5 years accuracy of the IntCal13 curve. D Calendric dates were calibrated using the atmospheric calibration curve IntCal09 for the Northern Hemisphere

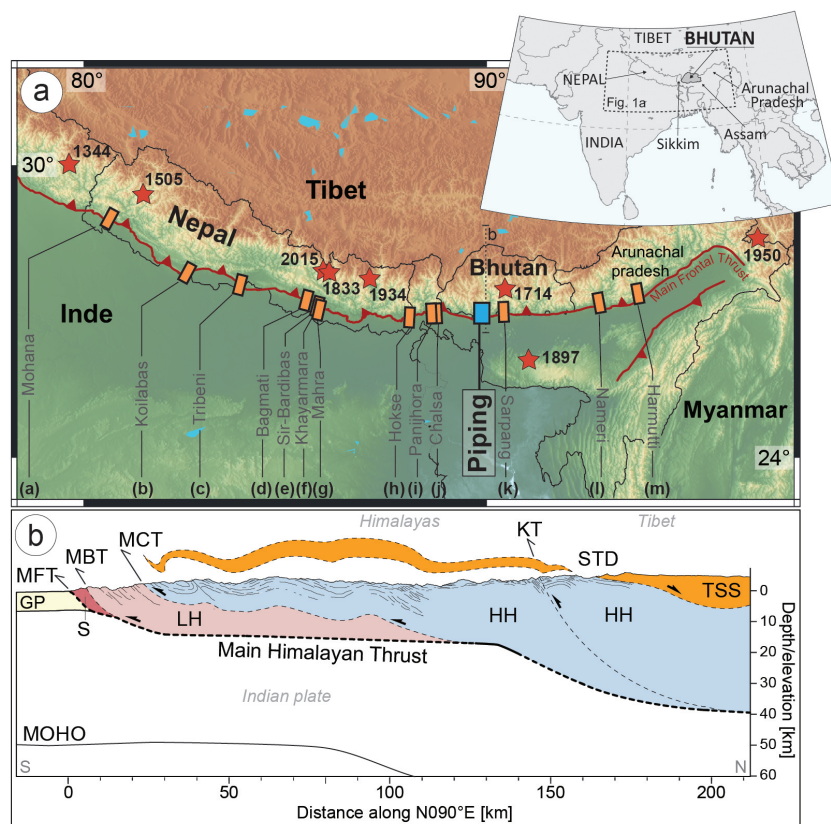


Figure 1

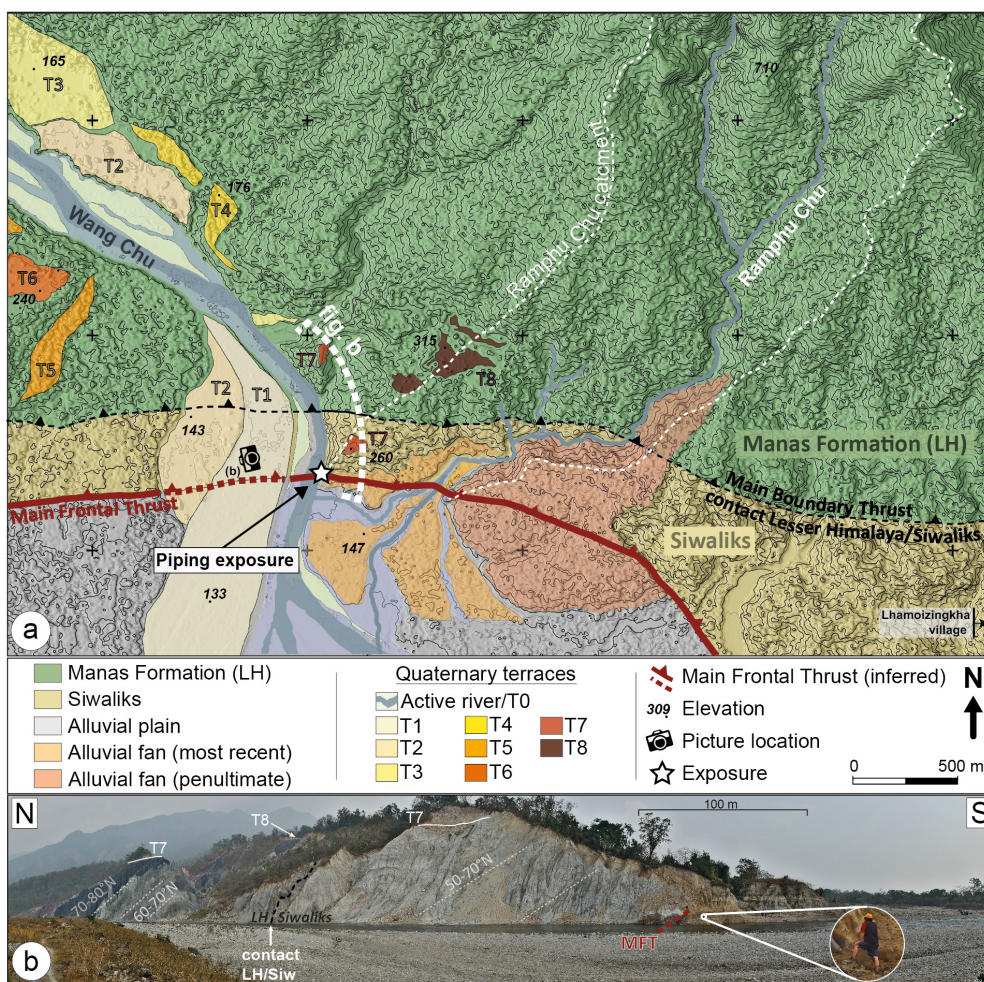


Figure 2

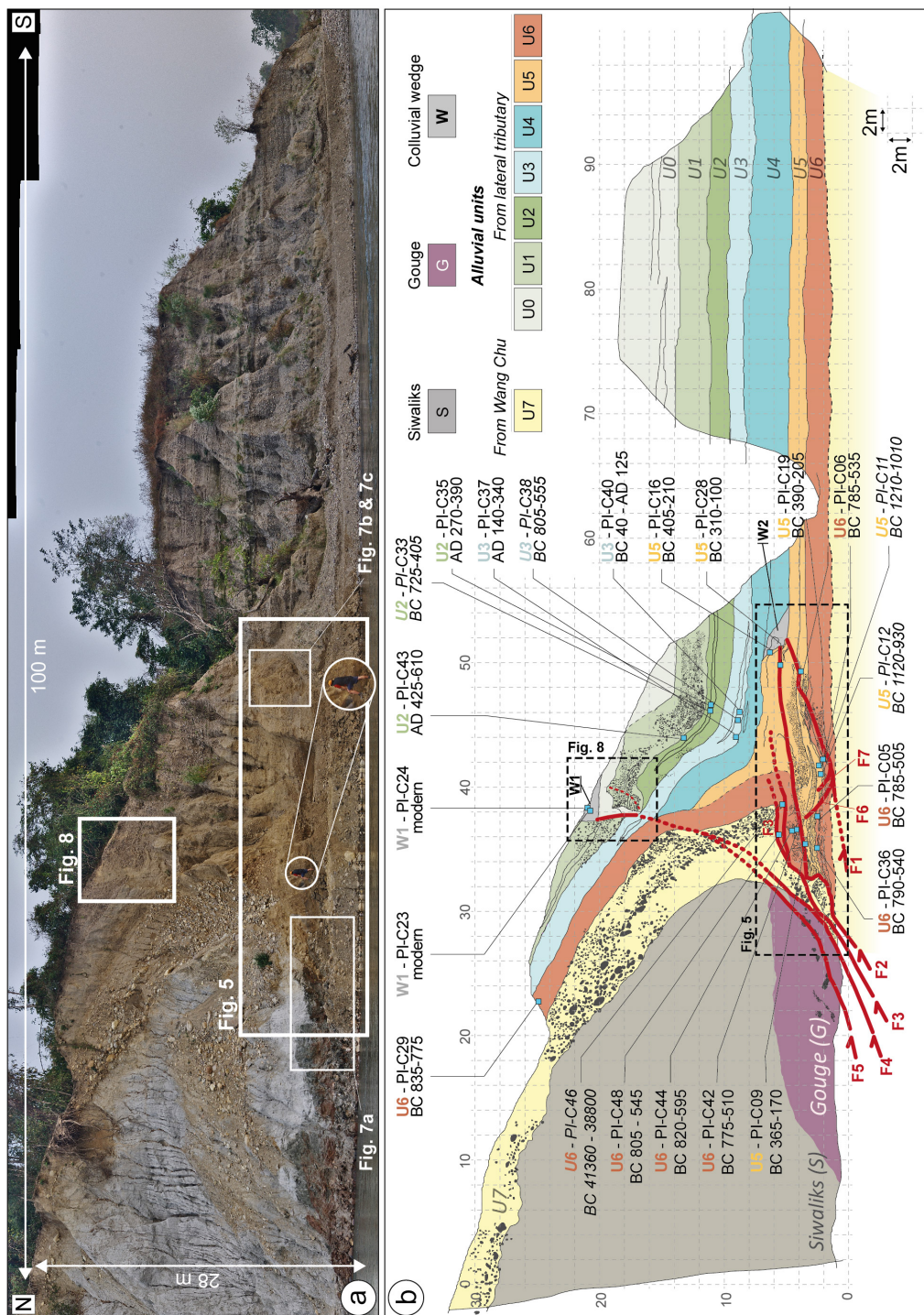


Figure 3

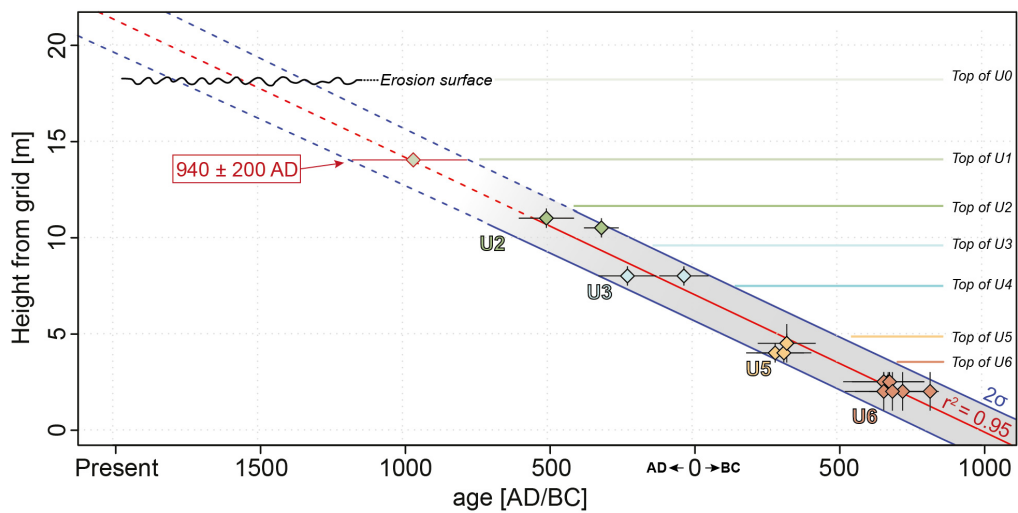


Figure 4

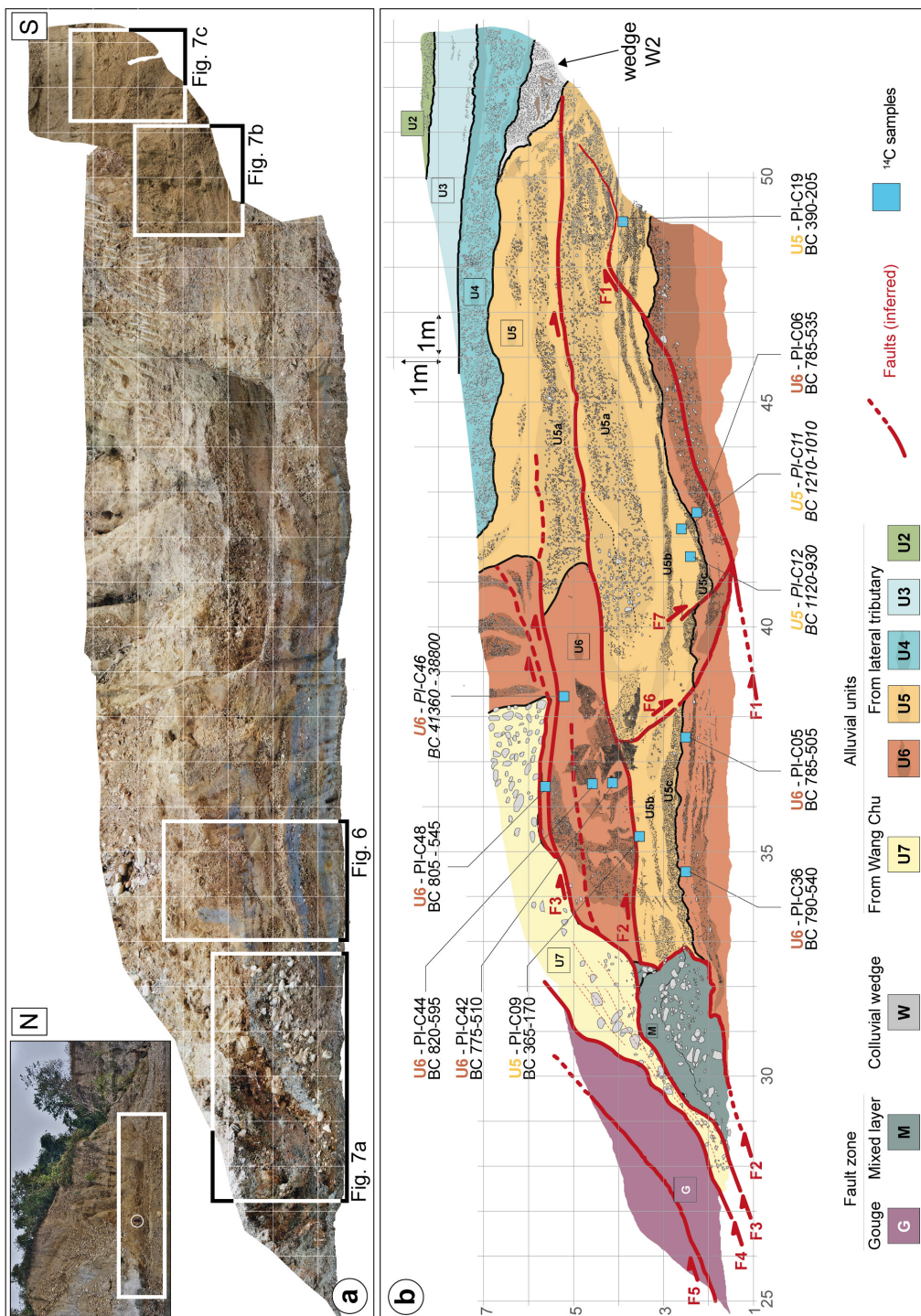


Figure 5



Figure 6

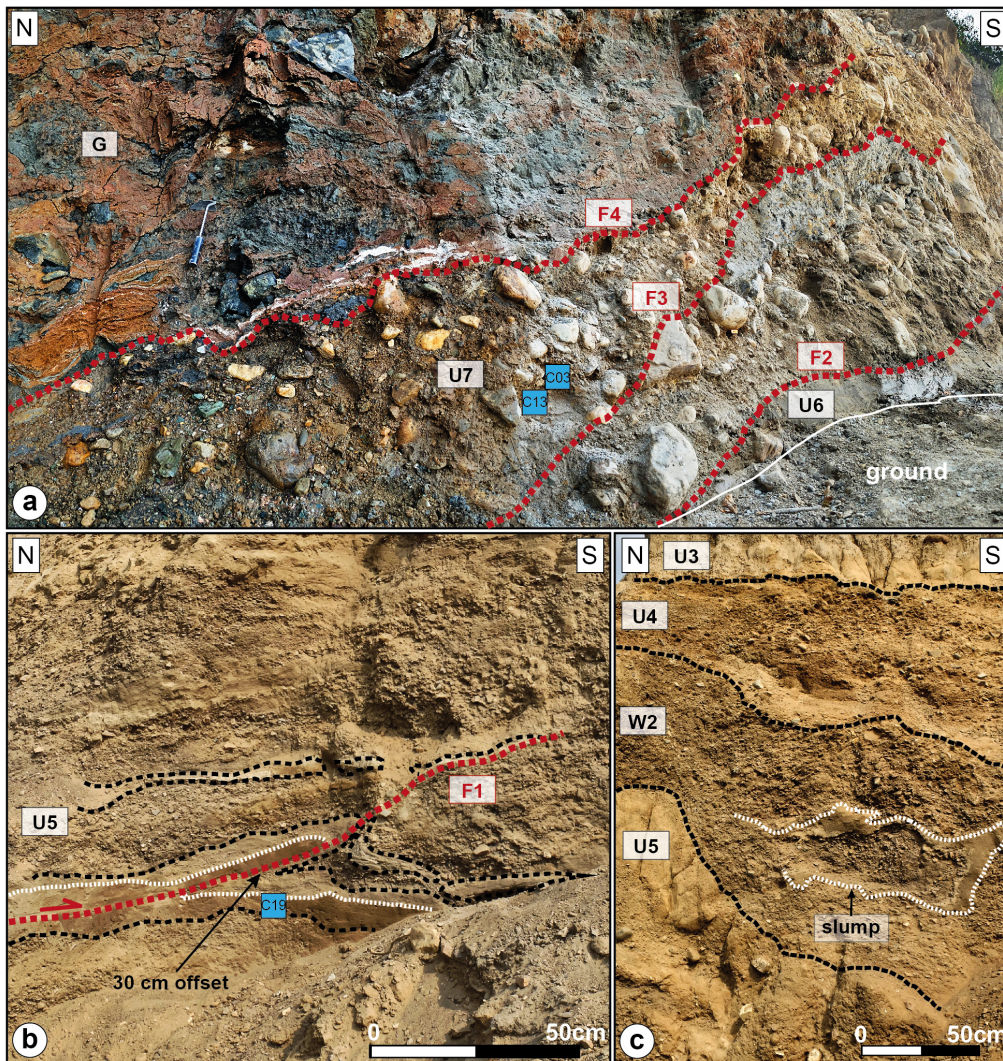


Figure 7

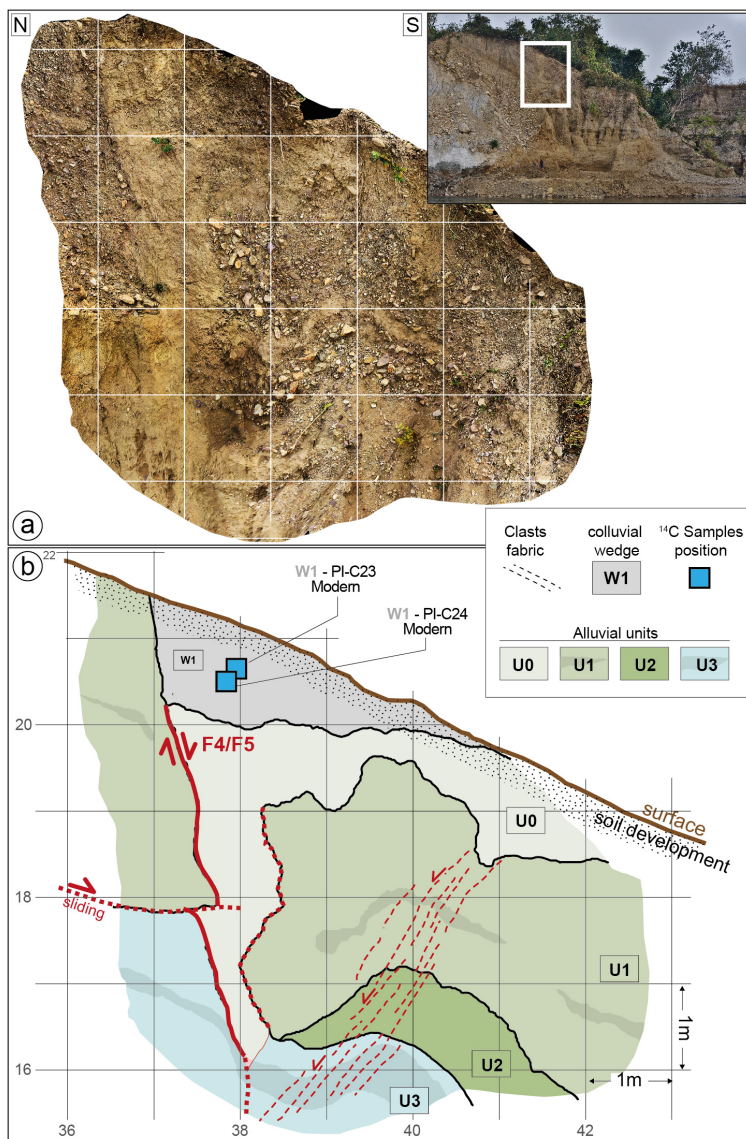


Figure 8

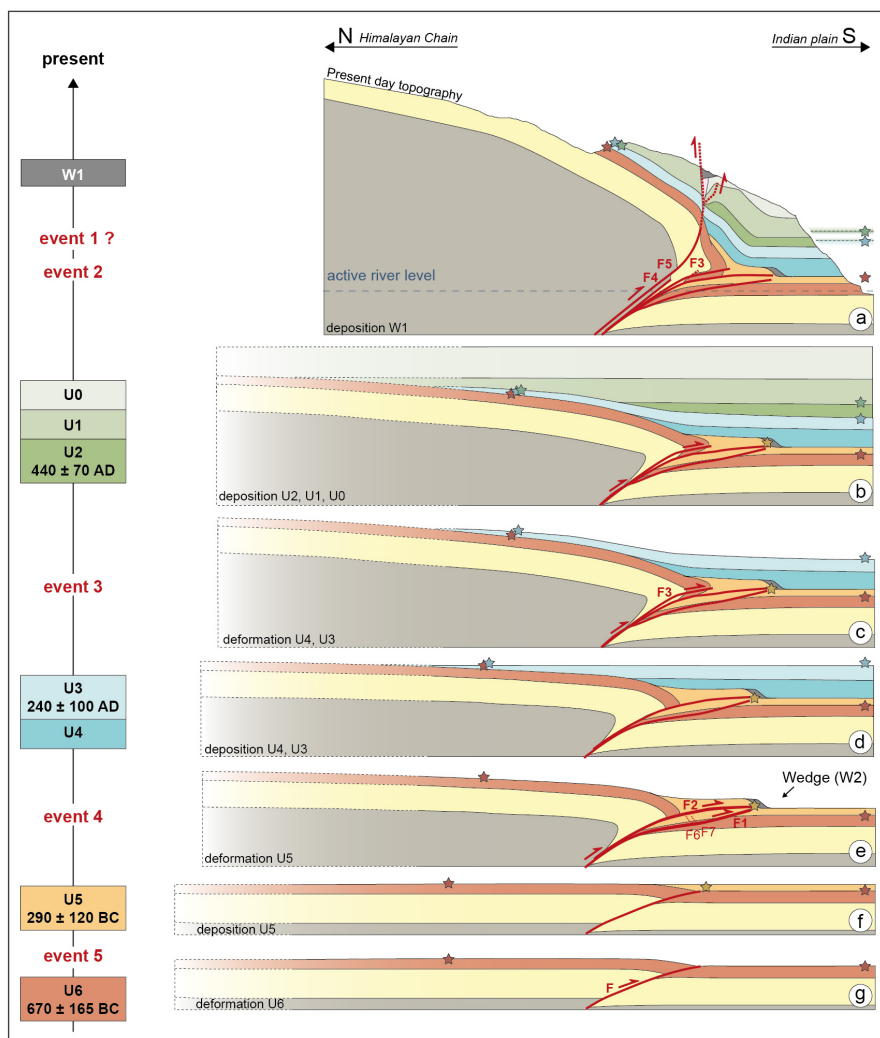


Figure 9

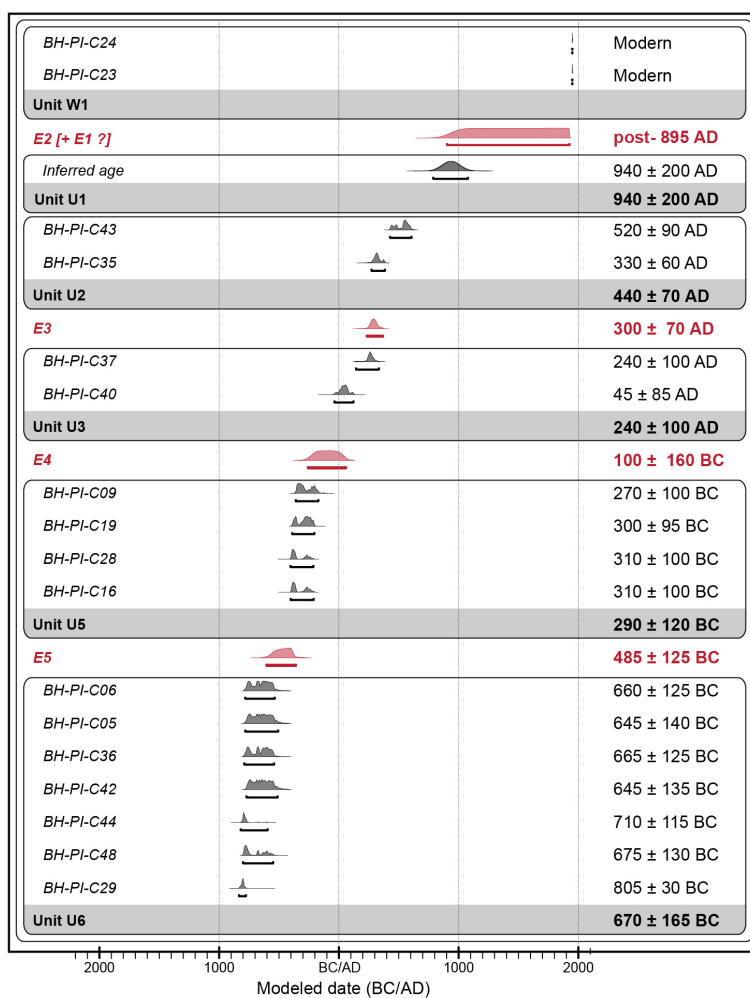


Figure 10

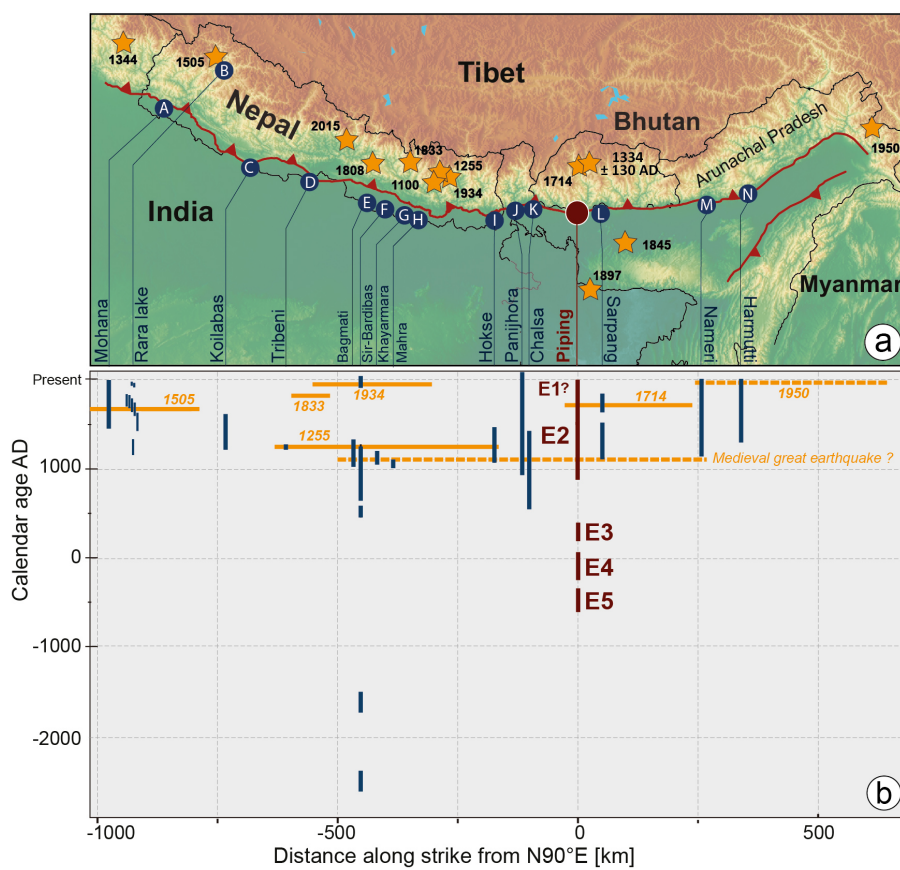


Figure 11